

DETECTION OF DISBONDING IN BONDED JOINTS WITH A SPATIALLY DISPLACED CFBG SENSOR

T.F. Capell¹, S.L. Ogin^{1*}, A.D. Crocombe¹, P. Peres², D. Barnoncel²

¹ Faculty of Engineering and Physical Sciences, University of Surrey, Guildford, UK,

² ASTRIUM Space Transportation, St Médard en Jalles, France

* Corresponding author (S.Ogin@surrey.ac.uk)

Keywords: *chirped fibre Bragg grating, NDT, composite materials*

1 Introduction

Optical fibre based sensors are being increasingly accepted by industry as an alternative to wire based strain gauges and are now available "off-the-shelf" [e.g. 1]. The fibre based sensors are regarded as intrinsically safe, light-weight and can be multiplexed, further reducing the mass of a distributed sensor system. Fibre Bragg grating sensors have been widely used to monitor strain in civil engineering structures [e.g. 2] and research has demonstrated their use for strain sensing and damage monitoring in composite structures [3,4,5].

This paper describes a study of the sensitivity of chirped fibre Bragg grating (CFBG) sensors to disbands in a generic bonded joint. In previous work, it has been shown unambiguously that an embedded sensor can detect the initiation and growth of a disbond when the sensor is located adjacent to the growing delamination/disbond. However, the spatial sensitivity of the sensor to a disbond in a remote part of the structure is unclear. Consequently, the focus of the current work is to investigate the sensor sensitivity to a disbond when the CFBG sensor is located in an undamaged part of the bonded joint. The complete study comprises virtual testing and experimental validation; this paper covers the theoretical part of the study, using a combination of finite element modelling and optical response modelling.

2 Virtual testing of a generic bonded joint

2.1 Structure of the bonded joint

The bonded joint was of the single lap type, joining two dissimilar composite adherends. A carbon fibre reinforced epoxy (CFRP) was used for the smaller adherend containing the CFBG sensor and glass

fibre reinforced epoxy (GFRP) was used for the larger adherend. A schematic of the joint can be seen in Figure 1.

The CFRP adherend was quasi-isotropic, having a lay-up ($\pm 45/0/90$)_s. For the experimental work, an out-of-autoclave pre-preg (obtained from Advanced Composites Group) was used to fabricate 200 mm x 200 mm panels containing the embedded CFBG sensors. Each ply was 0.25 mm thick. Adherends 30 mm wide were cut from the panel, and each adherend contained one CFBG sensor.

For the GFRP adherend, a cross ply GFRP laminate, (0_s/90/0₂)_s, was manufactured using a dry filament winding technique. A dry UD pre-form was prepared on a dedicated filament winding machine and this was then impregnated with a three part epoxy resin and cured in a press. Adherends 100 mm x 170 mm x 3 mm (width x length x thickness) were cut from the cured panel.

The joints were bonded using AV119, a single part heat-cured epoxy. The adhesive bond was controlled using PTFE sheet, 0.25 mm thick, which acted as an adhesive thickness end-fillet control. The end-fillet detail is shown in Figure 1; side fillets were controlled using 4 mm diameter PTFE rod to create a constant radius.

The bonded area of the joint was 40 mm x 30 mm, with a joint overlap of 50 mm. The 60 mm CFBG sensors extended from the right-hand end of the CFRP adherend in Figure 1, to a point 15 mm beyond the end of the bonded area.

2.2 Finite element analysis

For the first part of the virtual testing, a 3-dimensional model of the joint was constructed in Abaqus 6.9-1. The model used the same structure as the physical joint; it consisted of 3 separate parts that were assembled to form the complete joint.

Each of the fibre reinforced adherends were modelled as solid material, which was then divided into individual plies. The anisotropic material properties of each ply were assigned based on fibre orientation. The third part of the model, the adhesive, was modelled as an isotropic solid. The CFBG/optical fibre was not explicitly modelled, due to incompatibilities of scale, and the side adhesive fillet was also omitted.

The parts were meshed at part level using elements of the 3D stress type. Hexahedral elements (C3D8R) were used for the GFRP and the adhesive. The CFRP adherend used tetrahedral elements (C3D4). The mesh on the CFRP adherend included a small element size for the 60 mm length of adherend in the region of the CFBG sensor. The fine mesh was needed to generate sufficient data for the subsequent optical modelling work.

The three parts of the model were assembled using adhesive tie constraints and the disbanded area of the joint was controlled by removing the tie constraints, as required. Four sizes of disbonds are discussed in this paper, two having the form of a quarter circle and radii of 10 mm and 20 mm. The other two disbonds had quarter ellipse-shaped disbonds, with major and minor radii of (i) 20 mm and 10 mm, and (ii) 40 mm and 20 mm, respectively. The disbond was positioned at the boundary of the adhesive and the GFRP panel.

The boundary conditions applied to the assembled joint were as follows: The end of the GFRP panel was held *encastre*; the end of the CFRP panel was constrained to remain in-plane; a 5.4 kN tensile load was applied to the CFRP adherend in the plane of the joint (Figure 1), equivalent to a stress of 90 MPa for the CFRP adherend.

After analysing each model, longitudinal strains were extracted from paths which are candidate CFBG sensor positions. The number of data points along each 60 mm path varied between 350 to 1360, with a mean number of points of 852.

2.3 Optical modelling

The optical predictions were performed using OptiGrating, a fibre Bragg grating modelling software. The strains from the finite element models were first processed to produce a grating spacing, using a simple Excel spreadsheet (following Takeda et al [4]). The grating spacings were imported into the prediction software, which produced reflected

spectra. Predictions were made for both sensor orientations, either with the disbond located at the low wavelength end of the spectrum, or with the disbond located at the high wavelength end of the spectrum.

3 Results

3.1 Introduction

Nine candidate CFBG locations were investigated for each disbond configuration, giving a total of 36 strain profiles and 72 predicted spectra. The nine paths consisted of 3 locations through the thickness of the CFRP adherend and 3 across the width of the adherend. The paths are shown schematically in Figure 2. For the through-thickness locations, path *u* is the surface strain, path *v* is the strain within the 0° ply, and path *w* is the path through the 0° ply closest to the adhesive layer. For the width locations, path *x* is 12.5 mm from the top edge of the CFRP coupon (as shown in Fig. 2), path *y* is along the centre line of the CFRP adherend, and path *z* is 22.5 mm from the top edge of the CFRP coupon (consequently, 7.5 mm from the bottom edge). The 4 disbond sizes are shown schematically in Fig. 3, with the two quarter-circle disbonds labelled 1a and 1b (respectively), and the two ellipse-shaped disbonds being 2a and 2b, respectively. When identifying the disbond and the path of the strain being sampled, the convention is as follows: (i) disbond shape; (ii) position through the thickness; (iii) position across the width. One final identifying feature is the CFBG sensor orientation, since the sensor can be oriented with either the high-wavelength end (labelled "high") or the low-wavelength end (labelled "low") adjacent to the disbond. As an example of the use of this identifying convention, the spectrum prediction for path "1b-v-y-high" is the spectrum predicted for model 1b, (i.e. a 20 mm radius quarter circle), in the *v* position (i.e. 1.64 mm from the disbond interface), along the centre of the CFRP coupon (i.e. 15 mm from the edge of the adherend), and with the disbond located at the high wavelength end of the sensor.

3.2 10 mm quarter circle disbond

Figure 4 shows the strain profiles for the "w" path in model 1a for all the across-width possibilities (i.e. *x*, *y* and *z*). The disbond is a 10 mm radius quarter circle. These strain profiles are shown together with the strain profile from an undamaged joint (the

“NoDisbond” case). The “w” path is 0.85 mm away from the disbond in the through thickness direction; the positions within the width (i.e. the x, y and z-locations) are shown in the inset of Figure 4.

Comparing the strain profiles from the disbonded joint with the “NoDisbond” profile, there is little change in the profile away from the disbond end of the CFRP adherend, i.e. for 0.01 m and above. The inset shows the strain profiles for the first 15 mm of the CFRP adherend at a higher magnification, up to the end of the disbond. Not surprisingly, the paths further away from the disbond are similar to the NoDisbond case, and path lawx, which is closest to the edge of the disbond, shows the biggest change from the NoDisbond case.

Figure 5 shows part of the reflected spectra for joint 1a, when the high wavelength end of the sensor is located closest to the disbond. For CFBG spectra, perturbations in the reflected spectra are indicative of strain gradients. In Figure 5, the maximum point of the perturbation is shifted to a different wavelength in the predicted spectrum, depending on how well the CFBG sensor detects the disbond. Spectrum lawxhigh, a path that lies 2.5 mm outside of the disbonded area, shows a significant change in the peak wavelength of the perturbation compared to the NoDisbond case i.e. shift of 0.2 nm towards the low-wavelength end of the spectrum. It is likely that such a shift would be possible to detect experimentally (an FBG interrogator typically has a resolution of 0.01 nm). On the other hand, path lawyhigh (5 mm from disbond) shows a smaller shift and the peak in lawzhigh (12.5 mm from the disbond) is very close to the NoDisbond case. This indicates that for this size of damage, the disbond has to grow to within 5 mm of the CFBG path to be detected.

Figure 6 shows the predictions for the same paths, but now with the disbond located at the low wavelength end of the sensor. The disbond location is now indicated by a trough in the spectrum. Only the x path predicted spectrum shows a significant change (i.e. the path that is 2.5 mm from the disbond edge). From this, it can be concluded that the sensor orientation for improved sensitivity has the high-wavelength end near the disbond.

3.3 20 mm quarter circle disbond

Figure 7 shows the longitudinal strain as a function of distance in a joint with a 20 mm quarter circle

disbond. The strains have been extracted from the “w” through thickness position, i.e. the same as in section 3.2. With this larger disbonded area, now two paths, x and y, extend across the disbond front into the disbonded region and large strain changes can be seen moving from the disbonded to the bonded region. Path z, at a distance of 22.5 mm across the joint, is in a region beyond the edge of the disbond, but shows a change in the strain profile compared to the “no disbond” case, with the strain being compressive for the first 5 mm.

Figure 8 shows the predicted spectra based on the strain data of Fig. 7. The two paths that cross the disbond front (i.e. x and y) show peaks in the spectra corresponding to the disbond front position, as expected from previous work [e.g. 5]. Path z, which is beyond the edge of the disbond front, shows a shift in the position of the peak in the spectrum when compared with the “no disbond” case. This shift, of about 0.2 nm is likely to be detectable as a change within the measured CFBG reflected spectra, again suggesting that the CFBG sensor should be able to detect a disbond 2.5 mm away from the sensor.

3.4 Elliptical disbonds

Figure 9 shows the predicted spectra for an elliptical disbond 20 mm in length. The strains for the w paths are shown (which are 0.85 mm in the through-thickness direction from the disbond). For these results, the disbond was located at the high wavelength end of the CFBG sensor.

For this elliptical disbond, the spectra for both paths x and y show distinct changes i.e. for paths which are 2.5 mm and 5 mm from the edge of the disbond, and path z which is 12.5 mm from the disbond edge shows a perturbation which is similar to the NoDisbond case, as expected from the previous results.

In Figure 10, the spectra for the wx path for models 1a and 2a (the quarter circle and ellipse) have been plotted, along with the spectrum for a joint without a disbond. This is the path which is 2.5 mm from the edge of the disbond and, as shown above, the sensor can detect the presence of the disbond. However, this comparison shows that although the perturbation changes shape slightly for these two differently shaped disbonds, the wavelength of the maximum of the perturbation does not change significantly and it is likely to be difficult to differentiate between the

DETECTION OF DISBONDING IN BONDED JOINTS WITH A SPATIALLY DISPLACED CFBG SENSOR

quarter-circle and elliptical disbands.

4 Concluding remarks

This paper has described part of a study on the sensitivity of CFBG sensors to disbands in a generic bonded joint when the disbond front does not cross the path of the CFBG sensor. The study was carried out using virtual testing i.e. a combination of finite element analysis and reflected spectra predictions.

The study has shown for the first time that a CFBG sensor can detect a disbond that does not cross the path of the sensor. The modelling suggests that the CFBG sensor is slightly less sensitive to disbands when they are located in the vicinity of the low wavelength end of the CFBG sensor. The sensitivity of the sensor to the presence of a disbond is dependent on the local strain changes produced by the disbond to the joint under consideration. For the configuration of the generic joint used in this work, the results suggest that a CFBG sensor can monitor a region 2.5 mm either side of the sensor path with a reasonable expectation of detecting a disbond. For disbands located at the high wavelength end of the sensor, there is a reasonable expectation of detecting a disbond located within 5 mm of the sensor path. A series of experiments is in progress to validate the virtual testing presented in this paper.

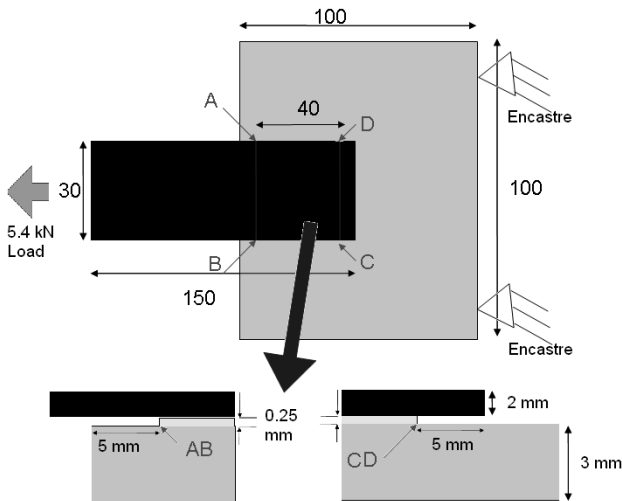


Fig.1. Schematic of joint, including bonding details and load. All dimensions in mm.

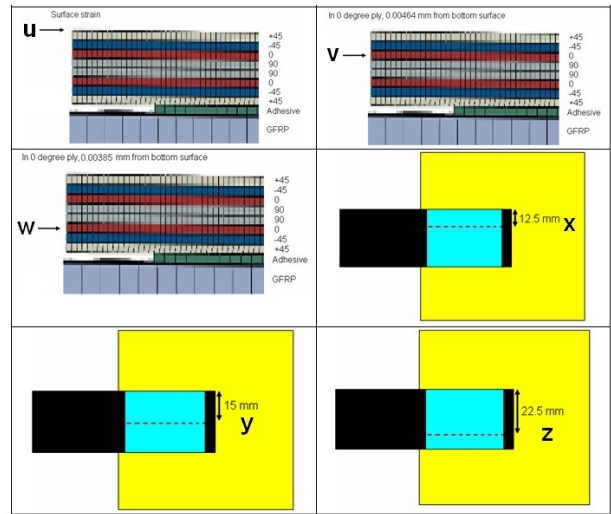


Fig.2. Matrix of possible CFBG paths. A total of 9 paths are available for each disbond shape.

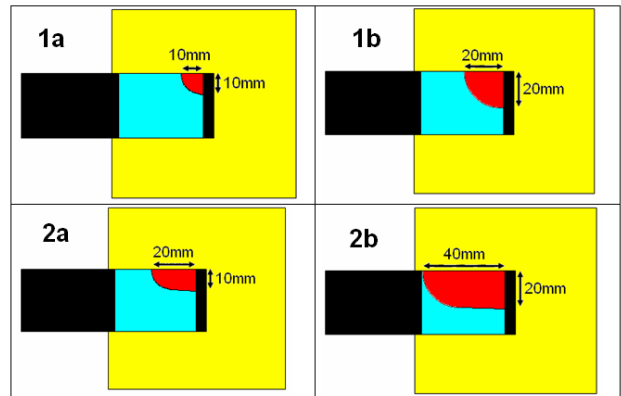


Fig.3. Matrix of disbond shapes, all dimensions in mm.

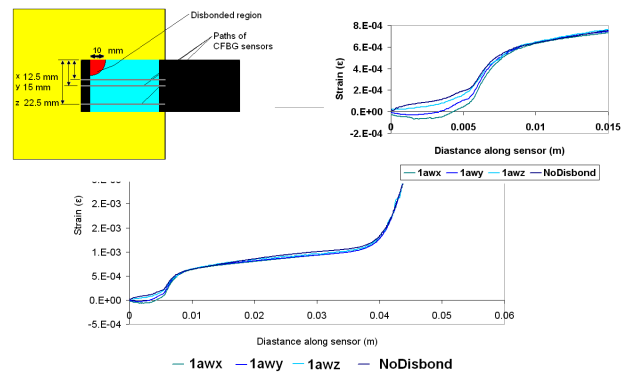


Fig.4. Strains in the joint along CFBG paths "w" for disbond geometry 1a. The inset shows the joint configuration (0 mm is at the cut end of the CFRP adherend)

DETECTION OF DISBONDING IN BONDED JOINTS WITH A SPATIALLY DISPLACED CFBG SENSOR

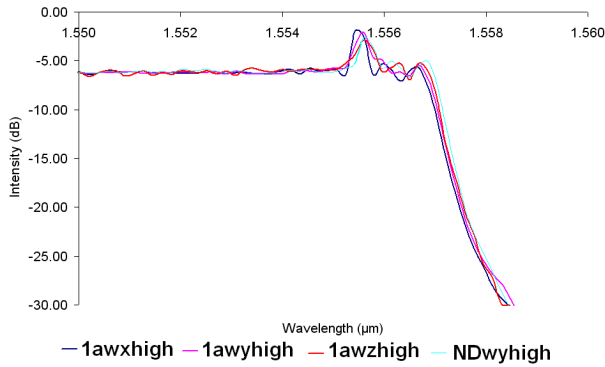


Fig. 5. Predicted spectra for a joint with a 10 mm quarter circle disbond and "no disbond"; the disbond is located at the **high** wavelength end of the spectrum

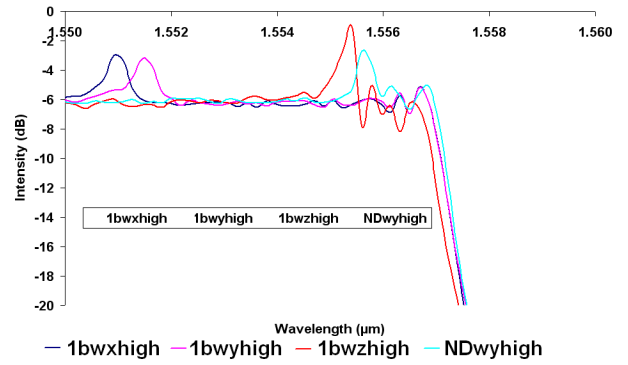


Fig. 8. Predicted spectra for a joint with a 20 mm quarter circle disbond and "no disbond"; note that the high-wavelength end of the spectrum corresponds to 0 mm in Figure 7.

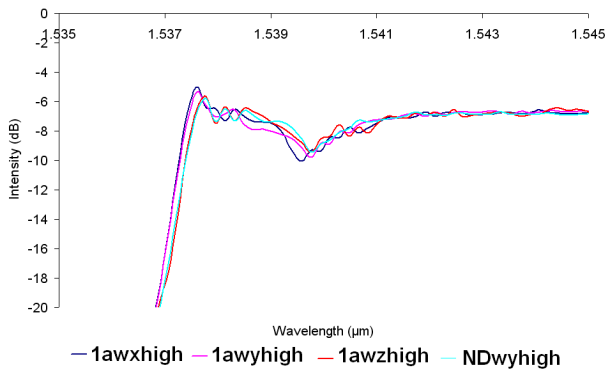


Fig. 6. Predicted spectra for a joint with a 10 mm quarter circle disbond and "no disbond"; the disbond is located at the **low** wavelength end of the spectrum

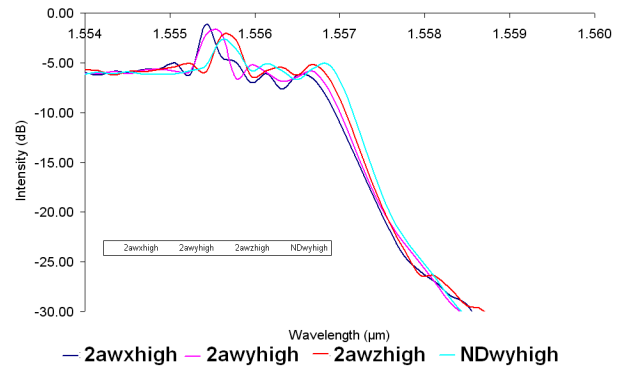


Fig. 9. Predicted spectra for model 2a, an ellipse disbond, for the w paths and the disbond located at the high wavelength end of the spectra.

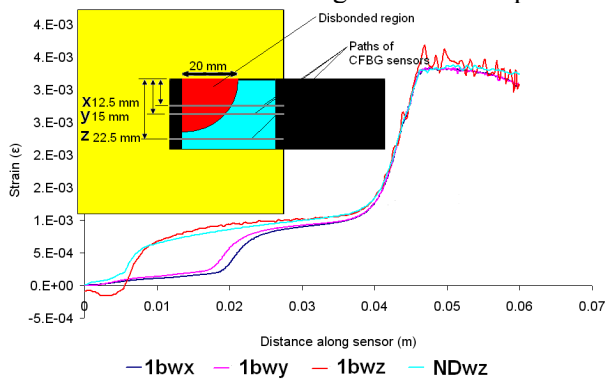


Fig. 7. Strains in the joint along elected CFBG paths. The inset shows the joint configuration (0 mm is at the cut end of the CFRP adherend).

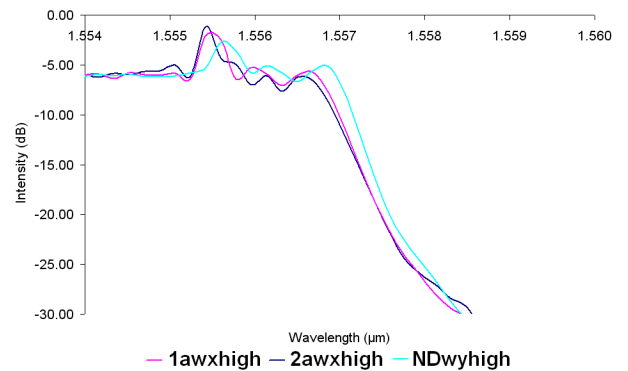


Fig. 10. Predicted spectra for paths 1awxhigh and 2awxyhigh compared to a "no disbond" spectrum for the disbond at the high wavelength end.

References

- [1] http://www.otland.com/SensorProducts/sensor_strain.html, accessed 25.5.2011.
- [2] Y.M. Gebremichael, W. Li, W.J.O. Boyle, B.T. Meggitt, K.T.V. Grattan, B. McKinley, G.F. Fernando, G. Kister, D. Winter, L. Canning, S. Luke “Integration and assessment of fibre Bragg grating sensors in an all-fibre reinforced polymer composite road bridge”. *Sensors and Actuators*; A118, pp. 78-85, 2005.
- [3] K. Lau, L. Yuan, L. Zhou, J. Wu, C. Woo “Strain monitoring in FRP laminates and concrete beams using FBG sensors”. *Composite Structures*, 51, pp 9-20, 2001.
- [4] N. Takeda, S. Yashiro, T. Okabe “Estimation of damage patterns in notched laminates with embedded FBG sensors”. *Composites Science and Technology*, 66, pp 684-93, 2006.
- [5] J. Palaniappan, S.L. Ogin, A.M. Thorne, G.T. Reed, T.F. Capell, S.C. Tjin, L. Mohanty “Disbond growth detection in composite–composite single-lap joints using chirped FBG sensors”, *Composites Science and Technology*, 68, pp 2410–17, 2008.